Photon-mediated long-range coupling of two Andreev pair qubits

L. Y. Cheung [1] ✉, R. Haller[1], A. Kononov [1] ✉, C. Ciaccia[1], J. H. Ungerer [1,2], T. Kanne[3], J. Nygård [3], P. Winkel [4,5,6], T. Reisinger [4], I. M. Pop [4], A. Baumgartner [1,2] & C. Schönenberger [1,2] ✉

When two superconductors are separated by a weak link, a supercurrent is carried by Andreev bound states formed by the phase-coherent reflection of electrons and their time-reversed partners. The two levels associated with a single, highly transmissive Andreev bound state can serve as a qubit due to the potentially large energy difference with the next bound state. Although coherent manipulation of these so-called Andreev pair qubits has been demonstrated, long-range qubit–qubit coupling, which is necessary for advanced quantum computing architectures, has not yet been achieved. Here, we demonstrate coherent remote coupling between two Andreev pair qubits mediated by a microwave photon in a superconducting cavity coupler. The latter hosts two modes that are engineered to have very different coupling rates to an external port. The strongly coupled mode can be used to perform a fast read-out of each qubit, while we use the weakly coupled mode to mediate the coupling between the qubits. When both qubits are tuned into resonance with the latter mode, we find excitation spectra with characteristic avoided crossings. We identify two-qubit states that are entangled over a distance of 6 mm. This work establishes Andreev pair qubits as a compact and scalable approach to developing quantum computers.

The fundamental quantum states in superconducting weak links are Andreev bound states (ABSs), which form as superpositions of propagating electrons and holes near a superconductor[1–3]. Figure 1a illustrates the formation of a single, highly transmissive ABS in a short normal metal or semiconductor region (N) between two superconducting reservoirs (S) with a superconducting gap Δ. The condition for constructive interference of the electron and hole partial waves contains phase shifts due to Andreev reflections at the N–S interfaces and the propagation in N[2,4,5]. For a single channel in the short junction limit, the constructive interference results in two time-reversed, spin-degenerate, Andreev levels, with eigenenergies tuned by the phase difference δ between the two superconducting order parameters. By including a transmission probability τ in the N part between the two superconductors, one obtains the energy spectrum $E_{\pm}(\delta) = \pm\Delta\sqrt{1-\tau\sin^2(\delta/2)}$ around the Fermi energy[6–10], as shown in Fig. 1b. We chose these two states at constant $\delta = \pi$ to define the Andreev pair qubit (APQ), which has a tunable excitation gap of $\Delta E = 2\Delta\sqrt{1-\tau}$. The APQ subspace is spanned by the even-parity ground state of the weak link and an excited state with two quasiparticle excitations. The corresponding qubit transition frequency is then given by $f_{qb} = \Delta E/h$, with the Planck constant h. As the next ABSs are typically found at much larger energies near Δ, the next excited state can, in principle, be engineered with a much greater energy difference than the qubit transition. This unique gate-tunable energy spectrum stands in strong contrast to other, more established superconducting qubits, for example,

[1]Department of Physics, University of Basel, Basel, Switzerland. [2]Swiss Nanoscience Institute, University of Basel, Basel, Switzerland. [3]Center for Quantum Devices, Niels Bohr Institute, University of Copenhagen, Copenhagen, Denmark. [4]IQMT, Karlsruhe Institute of Technology, Eggenstein-Leopoldshafen, Germany. [5]Departments of Applied Physics and Physics, Yale University, New Haven, CT, USA. [6]Yale Quantum Institute, Yale University, New Haven, CT, USA. ✉e-mail: lukyicheung@yahoo.de; artem.kononov@unibas.ch; christian.schoenenberger@unibas.ch

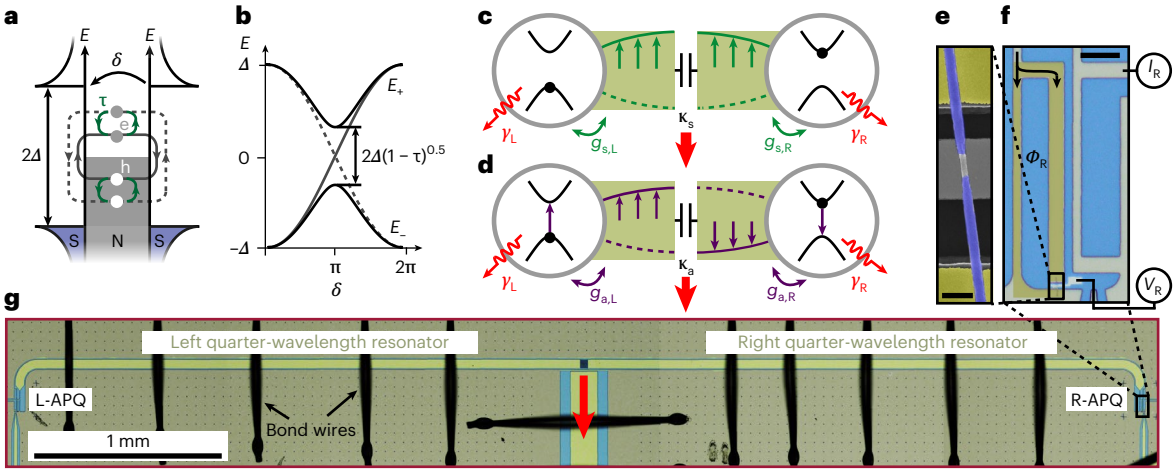

Fig. 1 | APQ coupling device. a, Formation of an ABS in an S-N-S weak link. In the N region, electron (e) and hole (h) partial waves can constructively interfere to form discrete subgap levels below the gap Δ. The phases of the partial waves obtain contributions from Andreev reflections at the N–S interfaces (curved grey lines) and from the propagation in the N region (horizontal grey lines). The two spin-degenerate and time-reversed trajectories can be coupled by single-particle scattering (green lines) with probability τ. **b**, The discrete Andreev levels $E_\pm(\delta)$ are plotted as a function of the phase difference δ between the two superconducting reservoirs. An energy gap of $2\Delta\sqrt{1-\tau}$ is opened by a finite τ at $\delta = \pi$. **c**,**d**, Schematics of the complete device containing two APQs (circles) with qubit decay rates $\gamma_{L/R}$ and APQ–coupler coupling strengths $g_{s/a,L/R}$ to the two cavity coupler modes. The symmetric mode (**c**, green) is used to read out qubit states, whereas the antisymmetric mode (**d**, purple) is used for coupling the two APQs, with mode-dependent coupling rate $\kappa_a \ll \kappa_s$ to the read-out port. **e**, Scanning electron micrograph of the R-APQ with epitaxially grown superconducting Al shell (purple) and suspended over a metallic bottom gate (grey). Scale bar, 300 nm. **f**, Optical micrograph of the qubit control lines. The junction is embedded in a radio-frequency SQUID (yellow) inductively coupled to the resonator. To maximize the mutual inductance, the end section of the resonator centre conductor was narrowed down and shared with the SQUID loop. The qubit frequency is controlled by a d.c. gate voltage V_R. The phase δ_R is generated by a d.c. current I_R in a flux line. Scale bar, 10 µm. **g**, Composite optical micrographs of the full device. It consists of two capacitively coupled quarter-wavelength coplanar transmission-line resonators (light green).

transmon qubits[11], in which dynamical driving of the qubits is severely limited by the leakage out of the computational subspace into higher excited states[12,13].

To implement a general quantum algorithm, it is necessary to couple two qubits coherently. Although the short-distance coupling between two ABSs over the superconducting coherence length is being explored in various systems[3,14,15], only a very recent report has demonstrated long-distance coupling over several tens of micrometres between two odd-parity Andreev states (Andreev spin qubits), which relies on a shared, strongly nonlinear mode[16]. The versatile long-distance coupling and quantum state read-out have been established for other qubit platforms, for example, superconducting[17] and semiconductor qubits[18,19], using superconducting microwave resonators. The reproducibility and low losses of superconducting microwave resonators and the potentially strong coupling to the APQs make these techniques ideal for transferring quantum information between APQs[20]. Despite substantial progress in understanding coupled ABS–resonator systems using circuit quantum electrodynamics, only experiments with single APQs have been performed so far[20–30].

Here, we employ a harmonic mode of a superconducting resonator to achieve strong remote coupling between two APQs over a distance of several millimetres. We first demonstrate the strong coupling of each individual APQ to the same superconducting resonator mode, with qubit decay rates lower than the coupling strengths. In a second step, we simultaneously bring both APQ transition energies into resonance with a specific resonator mode that couples only weakly to the measurement circuit. A coherent, exchange-type coupling between the two APQs is then established, with the mutual coupling mediated by a microwave photon and not disturbed by the out-coupling. The resulting excitation spectrum is fully captured by the Tavis–Cummings model[31] solely using independently determined, single-qubit parameters. This allows us to identify highly entangled two-qubit states and possibly allows the implementation of future remote two-qubit gate operations for Andreev qubits.

The quantum circuit investigated is illustrated schematically in Fig. 1c,d and consists of two InAs nanowire weak links, each with a single, highly transparent ABS forming the APQ. The nanowires have an epitaxially grown Al shell[32], which was etched away in a short semiconducting region to form the left APQ (L-APQ) and the right APQ (R-APQ). The local bottom gates are used to separately control the qubit frequency of each APQ. A scanning electron micrograph of the R-APQ is shown in Fig. 1e. This nanowire weak link is embedded in a superconducting pickup loop to form a radio-frequency superconducting quantum interference device (SQUID)[33], as shown in Fig. 1f. The threading magnetic fluxes $\Phi_{L,R} = \Phi_0\delta_{L,R}/2\pi$, which are controlled by external current lines, are used to set the corresponding phase differences $\delta_{L,R}$ over the two APQs, with $\Phi_0 = h/2e$ the superconducting flux quantum[20]. To achieve a coupling between the qubits, the pickup loops are inductively coupled to the centre conductor of the superconducting microwave resonator at two current antinodes (Fig. 1g). By design (Methods), this cavity coupler has two half-wavelength modes with different symmetries, one mode with a symmetric voltage profile along the transmission line with a resonance frequency of $f_s = 6.461$ GHz (Fig. 1c) and the other mode with an antisymmetric voltage profile with a resonance frequency of $f_a = 6.075$ GHz (Fig. 1d). To read out the resonator state, we designed an open-ended coplanar transmission line capacitively coupled to the very centre of the resonator. A radio-frequency voltage on this read-out port, thus, couples strongly to the symmetric coupler mode, with a coupling strength $\kappa_s/2\pi = 1.2$ MHz, whereas the same signal couples only very weakly to the antisymmetric mode.

We first demonstrate the strong coupling between each APQ and the antisymmetric coupler mode. Owing to the weak coupling to the read-out port, the antisymmetric coupler mode has a long lifetime and can strongly hybridize with an APQ at small detunings ($f_{qb} \approx f_a$). We probe the excitation spectra of the qubit–coupler hybrid system using pulsed two-tone spectroscopy. The transition from the ground state of the qubit–coupler system to an excited state can be addressed by an excitation pulse with variable microwave frequencies f_{drive}.

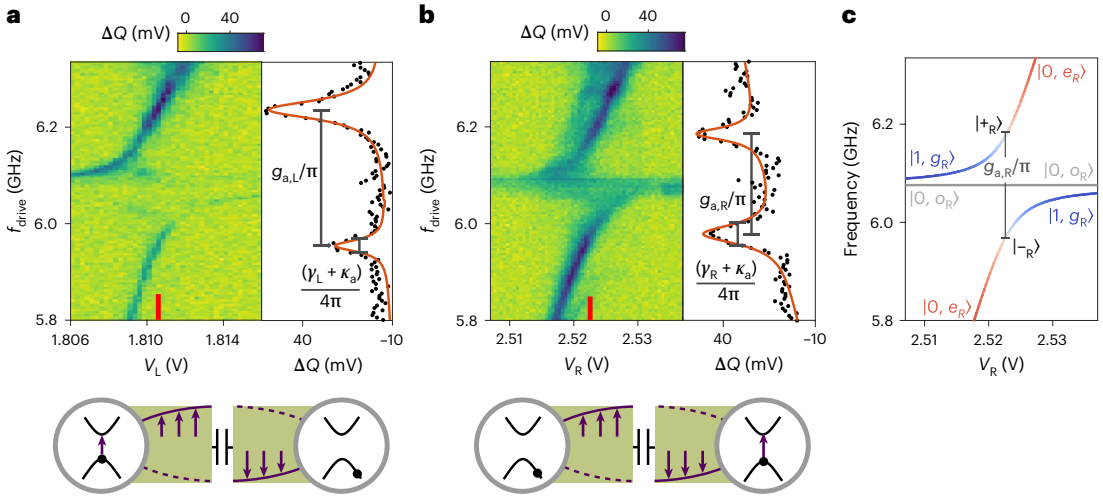

Fig. 2 | Strong coupling between individual APQs and the antisymmetric coupler mode. a, Differential quadrature ΔQ between the two reflected resonator probe pulses at f_s as a function of the qubit excitation frequency f_{drive} and V_L at $\delta_L = \pi$, which reveals an avoided crossing between the qubit and coupler resonances. The qubit–resonator coupling rate $g_{a,L}/(2\pi) = 141$ MHz and the qubit decay rate $\gamma_L/(2\pi) = 77$ MHz can be directly read out at $V_L = 1.810$ V, as illustrated in the cross section on the right of the plot. An illustration of the interaction between the resonator and the L-APQ is shown in the bottom inset. The interaction with the R-APQ was suppressed by tuning the R-APQ frequency to a larger value with $\delta_R = 1.2\pi$ while keeping $V_R = 2.5225$ V. **b**, Similarly, individual strong coupling between the R-APQ and the antisymmetric coupler mode was observed at $V_R = 2.5225$ V with $g_{a,R}/(2\pi) = 104$ MHz and $\gamma_R/(2\pi) = 82$ MHz. The horizontal resonance at $f_{drive} \approx 6.075$ MHz occurs through the occupation of the odd state due to quasiparticle poisoning. This resonance is missing in **a** because of the low excitation power seen by the circuit. **c**, Calculated excitation spectrum as a function of V_R using the listed parameters, which quantitatively reproduces the measured spectrum in **b**. The two resonances correspond to the qubit–coupler hybrid states $|\pm_R\rangle$, with the colour indicating the single-qubit weight $|\langle 0, e_R|\pm_R\rangle|^2$.

The population of such a hybrid excited state shifts the resonance frequency of the symmetric coupler mode, which is measured in the reflection coefficient of a microwave probe pulse at a frequency near f_s routed through a Josephson parametric amplifier operating close to the quantum limit[34]. The coupling strength between the symmetric coupler mode $g_{s,L/R}/(2\pi)$ and each APQ is independently found to be ~120 MHz (data not shown). In our experiment, both the qubit excitation and resonator probe pulses are routed through the read-out port to the qubit–coupler system. A differential measurement is obtained by applying the resonator probe pulse twice: during the qubit excitation and after the system has relaxed back to the ground state (details in Methods). The differential quadrature ΔQ is obtained by subtracting the two reflected signals to reject slow drifts.

To investigate a single APQ–coupler system, we tune the respective phase of the investigated APQ to the sweet spot $\delta_i = \pi$, where the qubit frequency is insensitive to small phase fluctuations. The other, idling APQ is phase biased such that its transition frequency is much larger than f_a. Figure 2a shows the differential quadrature ΔQ as a function of f_{drive} and V_L. We find an avoided crossing between the qubit and cavity resonances, which demonstrates the coherent coupling between the L-APQ and the antisymmetric coupler mode[35]. A fit of ΔQ on resonance, $f_a = f_{qb,L}$, with two Lorentzians and a linear background results in a qubit–coupler coupling rate of $g_{a,L}/(2\pi) = 141$ MHz, which exceeds the qubit decay rate $\gamma_L/(2\pi) = 77$ MHz. We find similarly strong qubit–resonator coupling for the R-APQ, with $g_{a,R}/(2\pi) = 104$ MHz and $\gamma_R/(2\pi) = 82$ MHz (Fig. 2b).

In addition to the avoided crossing for the R-APQ in Fig. 2b, we find a weak, gate-independent resonance at the frequency $f_a = 6.075$ GHz between the APQ–coupler hybrid states. We attribute this line to the excitation of the bare antisymmetric coupler mode without a coupled APQ. In the short junction limit, two degenerate, current-less, odd-parity states are insensitive to the resonator current and, thus, do not couple to the resonator[22]. By exciting the bare antisymmetric resonator mode, switching the parity at a rate faster than the measurement time could, therefore result in a reflected signal.

When a bare qubit state is degenerate with the cavity excitation, the exchange of excitations between them results in a new set of eigenstates, which is seen as an avoided crossing in the spectrum. The measured spectra are very well reproduced by the Jaynes–Cummings Hamiltonian[20,21,23,24,36] for one resonator mode coupled to a qubit: $H_{JC} = \hbar g_{a,i}(a\sigma_{+,i} + a^\dagger\sigma_{-,i})$, with σ_+ (σ_-) and $a^\dagger$ (a) the qubit and resonator photon raising (lowering) operators. This Hamiltonian describes the coherent exchange of an excitation between a qubit i and the cavity mode at a rate $g_{a,i}$. Figure 2c plots the corresponding calculated spectrum for the R-APQ as a function of V_R using the extracted $g_{a,R}$ (see Methods for details). The voltage axis is calibrated by equating the lowest and highest resonance frequencies with the corresponding qubit frequencies. The two resonances corresponding to the qubit–coupler hybrid states $|\pm_R\rangle$ are coloured according to the qubit weight $|\langle 0, e_R|\pm_R\rangle|^2$. As the R-APQ qubit frequency is tuned across f_a by V_R, the eigenstate $|+_R\rangle$ evolves gradually from a bare photonic state $|1, g_R\rangle$ to a bare qubit excited state $|0, e_R\rangle$, whereas $|-_R\rangle$ evolves from $|0, e_R\rangle$ to $|1, g_R\rangle$. At the degeneracy point at $V_R = 2.5225$ V, the coherent exchange of one excitation forms the two maximally hybridized states $|\pm_R\rangle = 1/\sqrt{2}(|1, g_R\rangle \pm |0, e_R\rangle)$, with a vacuum Rabi splitting of $g_{a,R}/\pi$. The odd state $|1, o_R\rangle$ does not couple to the resonator, so the resonance is purely given by the bare antisymmetric mode frequency f_a.

The main result of our work is shown in Fig. 3. We investigate the circuit with both qubit frequencies tuned into resonance with the antisymmetric coupler mode. First, the L-APQ–coupler maximally hybridized states $|\pm_L\rangle$ are generated by setting $V_L = 1.810$ V and $\delta_L = \pi$. Then, we again perform pulsed two-tone spectroscopy while sweeping V_R such that the qubit frequency $f_{qb,R}$ of the R-APQ crosses f_a. The differential quadrature ΔQ is plotted as a function of V_R and f_{drive} in Fig. 3a. The measurements exhibit a resonance evolving from $|-_L\rangle$ for $f_{qb,R} \ll f_a$ to $|+_L\rangle$ for $f_{qb,R} \gg f_a$. As the single-qubit frequency $f_{qb,R}$ is tuned into resonance with $|-_L\rangle$, the R-APQ hybridizes with the left-site coupled system to form an avoided crossing between the resonances of $|-_L\rangle$ and the R-APQ excited state. Likewise, a second avoided crossing emerges when $f_{qb,R}$ crosses the transition frequency to $|+_L\rangle$, giving rise to the

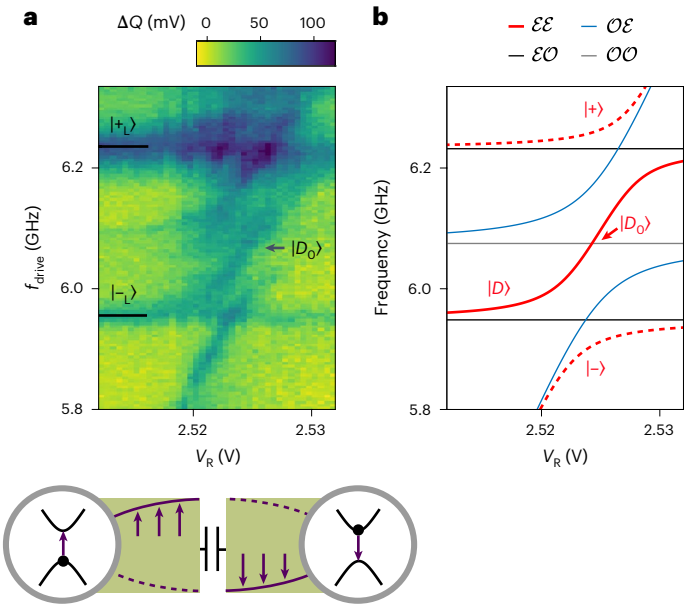

Fig. 3 | Remote coupling of two APQs. a, Differential quadrature ΔQ plotted as a function of V_R for both APQs tuned into resonance with the antisymmetric resonator mode ($\delta_L = \delta_R = \pi$ and $V_L = 1.810$ V). The states causing the individual resonances are identified in **b** and explained in the text. Most relevant is the resonance $|D\rangle$, which corresponds to a two-qubit hybrid state with an antisymmetric superposition of the two APQ excited states. The increased contrast for features at high f_{drive} is caused by the vicinity to the symmetric coupler mode frequency. **b**, Calculated excitation spectrum as a function of V_R using the Tavis–Cummings model with two qubits, one resonator mode and the parameters found independently in Fig. 2. The plotted spectrum contains excitation spectra of different parity configurations, where $\mathcal{E}$ ($\mathcal{O}$) denotes the even (odd) parity state of a single APQ, and the left (right) symbol labels the L-APQ (R-APQ). When one of the qubits is in the odd-parity state, the spectra reproduce the single-qubit characteristics shown in Fig. 2c. The dashed red lines correspond to the two hybrid states with a symmetric superposition of the two qubit states, whereas the solid line corresponds to the state with an antisymmetric superposition of the two qubit states.

sigmoid-like dispersion[18,19,37]. This resonance is characteristic of a two-qubit hybrid state $|D\rangle$ with an antisymmetric superposition of the two qubit states and demonstrates the strong coupling between the two APQs over a macroscopic distance.

To identify the eigenstates of the complete circuit, we calculate the excitation spectrum as a function of V_R using the Tavis–Cummings model $H_{TC} = \sum_i^N \hbar g_{a,i}(a\sigma_{+,i} + a^\dagger\sigma_{-,i})$ (ref. 31). This model describes the interaction between one resonator mode and $N > 1$ qubits. Inserting the qubit–resonator coupling rates extracted from the single-qubit measurements in Fig. 2, the resulting dispersion relation for the eigenstates reproduces the experiments very well (Fig. 3b). The solid red line indicates the transition to the excited state $|D\rangle$. This model now allows us to identify the eigenstates. The sigmoid-like resonance is a superposition of the two bare qubit excited states and the resonator state. When all three bare transition frequencies are resonant (arrows), the coherent exchange between the qubits results in an eigenstate $|D_0\rangle$ devoid of the photonic excitation. Explicitly, this state is

$$|D_0\rangle = \frac{1}{\sqrt{g_{a,L}^2 + g_{a,R}^2}}\left(g_{a,R}\,|0, e_L, g_R\rangle - g_{a,L}\,|0, g_L, e_R\rangle\right). \quad (1)$$

The dashed red lines are associated with transitions to the two 2-qubit hybrid states $|\pm\rangle$ with a symmetric superposition of the two APQ excited states. The existence of these strongly correlated quantum states

Table 1 | Coupling strengths used to calculate the excitation spectra for different parity configurations

Parity configurations	$g_{a,L}/(2\pi)$ (MHz)	$g_{a,R}/(2\pi)$ (MHz)
$\mathcal{EE}$	141	104
$\mathcal{EO}$	141	0
$\mathcal{OE}$	0	104
$\mathcal{OO}$	0	0

formed by the exchange of a cavity photon shows that both APQs, in the even parity $\mathcal{EE}$, coherently interact with an exchange-type coupling, which is the main result of this work. However, the spectrum is more complex and requires further consideration of parity-switching events.

Because parity-switching events are expected to occur locally and to be uncorrelated between the two APQs, four parity configurations could randomly occur during the measurement: a single APQ with odd parity and the other with even parity, denoted $\mathcal{OE}$ and $\mathcal{EO}$, and both APQs with odd or even parity, denoted $\mathcal{OO}$ and $\mathcal{EE}$, respectively. The calculated eigenenergies of the coupled system in the $\mathcal{OE}$, $\mathcal{EO}$ and $\mathcal{OO}$ configurations are shown in Fig. 3b. The corresponding coupling strengths are listed in Table 1. Because an APQ with odd parity is not coupled to the resonator, the spectra reproduce the single-qubit characteristics of the other qubit found in Fig. 2. Therefore, the parity configuration $\mathcal{EO}$ gives rise to two constant resonances associated with the transition to the states $|\pm_L\rangle$, which reproduces the cross section in Fig. 2a. The parity configuration $\mathcal{OE}$ adds an avoided crossing between the bare antisymmetric mode and the R-APQ excited state, reproducing Fig. 2b. These four resonances are seen in the experiment, showing that both APQs switch between different parities during the measurement time of 1.5 s. More data for an L-APQ slightly detuned from f_a, as plotted in Extended Data Fig. 1, can be reproduced in this model with the same device parameters, showing that this quantum system is very versatile, well controlled and well understood.

In summary, we demonstrate the remote coupling of two APQs over a distance of 6 mm, mediated by a specifically designed superconducting resonator with a strongly coupled mode and a weakly coupled mode for qubit read-out and qubit coupling, respectively. In the resonant regime, the corresponding eigenstates of the full hybrid circuit can be identified using independently determined parameters inserted into the Tavis–Cummings Hamiltonian with two qubits and one cavity mode. When all energies are degenerate, we find a maximally entangled two-qubit state, which is mediated by the cavity coupler. Our experiments are a proof of principle for cavity-mediated interactions between APQs. This approach may be useful for complex quantum computer architectures. Because of the spin-to-supercurrent conversion of an Andreev spin qubit, our cavity coupler, which inductively couples to the pickup loops containing the weak links, could be used to remotely couple Andreev spin qubits.

References

1. Andreev, A. F. Thermal conductivity of the intermediate state of superconductors. *Sov. Phys. JETP* **19**, 1228 (1964).
2. Kulik, I. Macroscopic quantization and the proximity effect in s-n-s junctions. *Sov. Phys. JETP* **30**, 944 (1970).
3. Jünger, C. et al. Intermediate states in Andreev bound state fusion. *Commun. Phys.* **6**, 190 (2023).

4. Jünger, C. et al. Spectroscopy of the superconducting proximity effect in nanowires using integrated quantum dots. *Commun. Phys.* **2**, 76 (2019).
5. Bagwell, P. F. Suppression of the Josephson current through a narrow, mesoscopic, semiconductor channel by a single impurity. *Phys. Rev. B* **46**, 12573–12586 (1992).
6. Zazunov, A., Shumeiko, V. S., Bratus', E. N., Lantz, J. & Wendin, G. Andreev level qubit. *Phys. Rev. Lett.* **90**, 087003 (2003).
7. Furusaki, A. & Tsukada, M. Current-carrying states in Josephson junctions. *Phys. Rev. B* **43**, 10164–10169 (1991).
8. Beenakker, C. W. J. & van Houten, H. Josephson current through a superconducting quantum point contact shorter than the coherence length. *Phys. Rev. Lett.* **66**, 3056–3059 (1991).
9. Furusaki, A. Josephson current carried by Andreev levels in superconducting quantum point contacts. *Superlattices Microstruct.* **25**, 809–818 (1999).
10. Despósito, M. A. & Yeyati, A. L. Controlled dephasing of Andreev states in superconducting quantum point contacts. *Phys. Rev. B* **64**, 140511 (2001).
11. Koch, J. et al. Charge-insensitive qubit design derived from the Cooper pair box. *Phys. Rev. A* **76**, 042319 (2007).
12. McEwen, M. et al. Removing leakage-induced correlated errors in superconducting quantum error correction. *Nat. Commun.* **12**, 1761 (2021).
13. Werninghaus, M. et al. Leakage reduction in fast superconducting qubit gates via optimal control. *npj Quantum Inf.* **7**, 14 (2021).
14. Su, Z. et al. Andreev molecules in semiconductor nanowire double quantum dots. *Nat. Commun.* **8**, 585 (2017).
15. Kürtössy, O. et al. Andreev molecule in parallel InAs nanowires. *Nano Lett.* **21**, 7929–7937 (2021).
16. Pita-Vidal, M. et al. Strong tunable coupling between two distant superconducting spin qubits. *Nat. Phys.* **20**, 1158–1163 (2024).
17. Majer, J. et al. Coupling superconducting qubits via a cavity bus. *Nature* **449**, 443–447 (2007).
18. Borjans, F., Croot, X. G., Mi, X., Gullans, M. J. & Petta, J. R. Resonant microwave-mediated interactions between distant electron spins. *Nature* **577**, 195–198 (2020).
19. van Woerkom, D. J. et al. Microwave photon-mediated interactions between semiconductor qubits. *Phys. Rev. X* **8**, 041018 (2018).
20. Metzger, C. et al. Circuit-QED with phase-biased Josephson weak links. *Phys. Rev. Res.* **3**, 013036 (2021).
21. Janvier, C. et al. Coherent manipulation of Andreev states in superconducting atomic contacts. *Science* **349**, 1199–1202 (2015).
22. Hays, M. et al. Direct microwave measurement of Andreev-bound-state dynamics in a semiconductor-nanowire Josephson junction. *Phys. Rev. Lett.* **121**, 047001 (2018).
23. Tosi, L. et al. Spin-orbit splitting of Andreev states revealed by microwave spectroscopy. *Phys. Rev. X* **9**, 011010 (2019).
24. Matute-Cañadas, F. J. et al. Signatures of interactions in the Andreev spectrum of nanowire Josephson junctions. *Phys. Rev. Lett.* **128**, 197702 (2022).
25. Pita-Vidal, M. et al. Direct manipulation of a superconducting spin qubit strongly coupled to a transmon qubit. *Nat. Phys.* **19**, 1110–1115 (2023).
26. Hays, M. et al. Coherent manipulation of an Andreev spin qubit. *Science* **373**, 430–433 (2021).
27. Hays, M. et al. Continuous monitoring of a trapped superconducting spin. *Nat. Phys.* **16**, 1103–1107 (2020).
28. Park, S. & Yeyati, A. L. Andreev spin qubits in multichannel Rashba nanowires. *Phys. Rev. B* **96**, 125416 (2017).
29. Cerrillo, J., Hays, M., Fatemi, V. & Yeyati, A. L. Spin coherent manipulation in Josephson weak links. *Phys. Rev. Res.* **3**, L022012 (2021).
30. Kurilovich, P. D., Kurilovich, V. D., Fatemi, V., Devoret, M. H. & Glazman, L. I. Microwave response of an Andreev bound state. *Phys. Rev. B* **104**, 174517 (2021).
31. Tavis, M. & Cummings, F. W. Exact solution for an *n*-molecule—radiation-field Hamiltonian. *Phys. Rev.* **170**, 379–384 (1968).
32. Krogstrup, P. et al. Epitaxy of semiconductor–superconductor nanowires. *Nat. Mater.* **14**, 400–406 (2015).
33. Tinkham, M. *Introduction to Superconductivity* 2nd edn (Dover Publications, 2004); www.worldcat.org/isbn/0486435032
34. Winkel, P. et al. Nondegenerate parametric amplifiers based on dispersion-engineered Josephson-junction arrays. *Phys. Rev. Appl.* **13**, 024015 (2020).
35. Blais, A., Grimsmo, A. L., Girvin, S. M. & Wallraff, A. Circuit quantum electrodynamics. *Rev. Mod. Phys.* **93**, 025005 (2021).
36. Jaynes, E. & Cummings, F. Comparison of quantum and semiclassical radiation theories with application to the beam maser. *Proc. IEEE* **51**, 89–109 (1963).
37. Fink, J. M. et al. Dressed collective qubit states and the Tavis–Cummings model in circuit QED. *Phys. Rev. Lett.* **103**, 083601 (2009).

Methods

Fabrication

Our device is fabricated on an undoped Si substrate with the native SiO_2 removed by a wet etch process using HF and piranha solutions[38]. We design and optimize the microwave circuit using Sonnet Suites and then pattern the cavity coupler and control lines by direct laser writing and reactive-ion etching of a sputtered NbTiN thin film. The latter has a thickness of 85 nm with a sheet kinetic inductance of 2.4 pH. Ti/Pd (5 nm/25 nm) metallic gate structures are fabricated by e-beam lithography and e-beam metal evaporation. Next, wurtzite InAs nanowires with a 30-nm-thick epitaxial Al full shell are suspended across the gap in the NbTiN layer using a micromanipulator. The segment of the Al shell suspended over the gate structures is then removed by an 18-s-long etch step in Transene type D. The left junction is 190 nm long and the right junction 280 nm. The nanowires are in contact with the rest of the circuit through a 125-nm-thick Al layer produced after 27 s of in situ Ar-milling. The Al is evaporated at a substrate temperature of −20 °C to reduce the granularity of the Al film. Because the loop inductance is much smaller than the junction inductance, the phase difference induced by the magnetic flux mostly drops across the junction, such that $\Phi_{L,R} = \Phi_0\delta_{L,R}/2\pi$, with $\Phi_0 = h/2e$ the superconducting flux quantum.

Superconducting microwave cavity coupler

The cavity coupler can be best understood as being composed of two nominally identical quarter-wavelength coplanar transmission-line resonators, with strong capacitive coupling at the respective voltage antinodes and a designed capacitance of 43 pF. This design couples the two quarter-wavelength modes of the individual coplanar transmission-line resonators into two half-wavelength modes, one in a symmetric and one in an antisymmetric combination. In addition, the coupling capacitor prohibits low-frequency dissipative currents from flowing through the centre conductor, thereby reducing internal losses. The coupling rate of the resonator modes into the read-out port depends on the design of the port. We use a single-ended, capacitively coupled read-out port at the centre of the resonator. This results in symmetric resonator fields with zero phase difference across the capacitor coupling to the measurement circuit with a designed, relatively large coupling rate κ_s. Moreover, the coupling rate of the antisymmetric mode κ_a is considerably smaller, due to the voltage symmetry mismatch (Extended Data Fig. 2).

Pulsed two-tone spectroscopy

To perform the differential two-tone spectroscopy described in the main text, we apply two-stage microwave pulses to the read-out port to excite the qubit and as a coupler probe (Extended Data Fig. 3). During the excitation stage, a strong excitation pulse and a weak coupler probe pulse are switched on simultaneously for 8 µs. The microwave frequency of the excitation pulse f_{drive} is varied to obtain the measured spectra described in the main text. The probe pulse is composed of four 2 µs pulses at a microwave frequency of ~6.461 GHz. The pulse length of 2 µs for a single read-out pulse is imposed by the hardware. This signal reflects from the coupler and is directed through a dimer Josephson-junction-array amplifier[34], a low-temperature, high-electron-mobility transistor, and a room-temperature amplifier before data acquisition. During the relaxation stage, the microwave pulses are switched off for 8 µs so that the system can relax to the ground state. A weak probe pulse is subsequently applied, reflected and acquired to probe the ground state of the hybrid circuit. Finally, the differential quadrature ΔQ between the two reflected probe pulses is computed and plotted as the spectra shown in the main text.

Calculating the excitation spectrum of the Tavis–Cummings model

For the single APQ–coupler system (Fig. 2c), we use the Hamiltonian

$$H_{N=1} = hf_a a^\dagger a + \frac{hf_{qb,R}}{2}\sigma_{z,R} + \hbar g_{a,R}\left(a\sigma_{+,R} + a^\dagger\sigma_{-,R}\right), \quad (2)$$

with $\sigma_{z,R}$ the qubit Pauli z-operator for the R-APQ. The resonance frequency of the antisymmetric mode f_a and the qubit–resonator coupling strength $g_{a,R}$ are extracted from Fig. 2b. The gate voltage dependence of the qubit frequency $f_{qb,R}(V_R)$ is obtained by linearly interpolating the measured transition frequencies to $|\pm_R\rangle$ at the far-resonant points, at which the hybrid state mainly consists of the qubit excited state. The Hamiltonian is numerically diagonalized to obtain its eigenenergies. To account for the decoupled odd-parity state, the eigenenergies are calculated with $g_{a,R} = 0$ and the spectrum is overlaid on top of that of the even-parity eigenenergies.

For the full hybrid circuit discussed in Fig. 3b, the Hamiltonian

$$H_{N=2} = hf_a a^\dagger a + \sum_{i\in L,R}\left[\frac{hf_{qb,i}}{2}\sigma_{z,i} + \hbar g_{a,i}(a\sigma_{+,i} + a^\dagger\sigma_{-,i})\right] \quad (3)$$

is diagonalized separately for the four sets of parameters so that we can compute the excitation spectra for the four different parity configurations. The four spectra are then overlaid to obtain Fig. 3b. The corresponding coupling strengths are listed in Table 1.

Data availability

All data in this publication are available in numerical form via Zenodo at https://doi.org/10.5281/zenodo.10037256 (ref. 39).

References

38. Ungerer, J. H. et al. Performance of high impedance resonators in dirty dielectric environments. *EPJ Quantum Technol.* **10**, 41 (2023).
39. Cheung, L. Y. & Kononov, A. Data for 'Photon-mediated long-range coupling of two Andreev pair qubits'. *Zenodo* https://doi.org/10.5281/zenodo.10037256 (2024).

Acknowledgements

We thank P. Krogstrup for assistance with material growth. We thank J. Ridderbos, M. Goffman and H. Pothier for advice on the microwave measurement. We thank A. Levy Yeyati and F. Matute-Cañadas for scientific discussions about the physics of ABSs. We thank N. Zapata for assistance with the fabrication and characterization of the Josephson-junction-array amplifier. This research was supported by the European Union's Horizon 2020 research and innovation programme through the FET-open project AndQC (Agreement No. 828948) and the Marie Skłodowska-Curie COFUND project QUSTEC (Agreement No. 847471). It was also supported by the Swiss National Science Foundation (Grant No. 192027), the Spin Qubit in Silicon programme of the National Centre of Competence in Research and the Swiss Nanoscience Institute. T.K. and J.N. acknowledge financial support from the Novo Nordisk Foundation SolidQ project and the Danish National Research Foundation (Grant No. DNRF 101).

Author contributions

L.Y.C. fabricated the quantum circuitry with the help of R.H., A.K. and J.H.U. C.C. fabricated the parametric amplifier with the assistance of P.W., T.R. and I.M.P. L.Y.C., R.H. and A.K. performed the measurements. L.Y.C. and A.K. analysed the data with inputs from R.H., A.B. and C.S. L.Y.C. wrote the manuscript with inputs from all authors. C.S. initiated the project. T.K. and J.N. developed the nanowire materials.

Competing interests

The authors declare no competing interests.

Correspondence and requests for materials should be addressed to L. Y. Cheung, A. Kononov or C. Schönenberger.

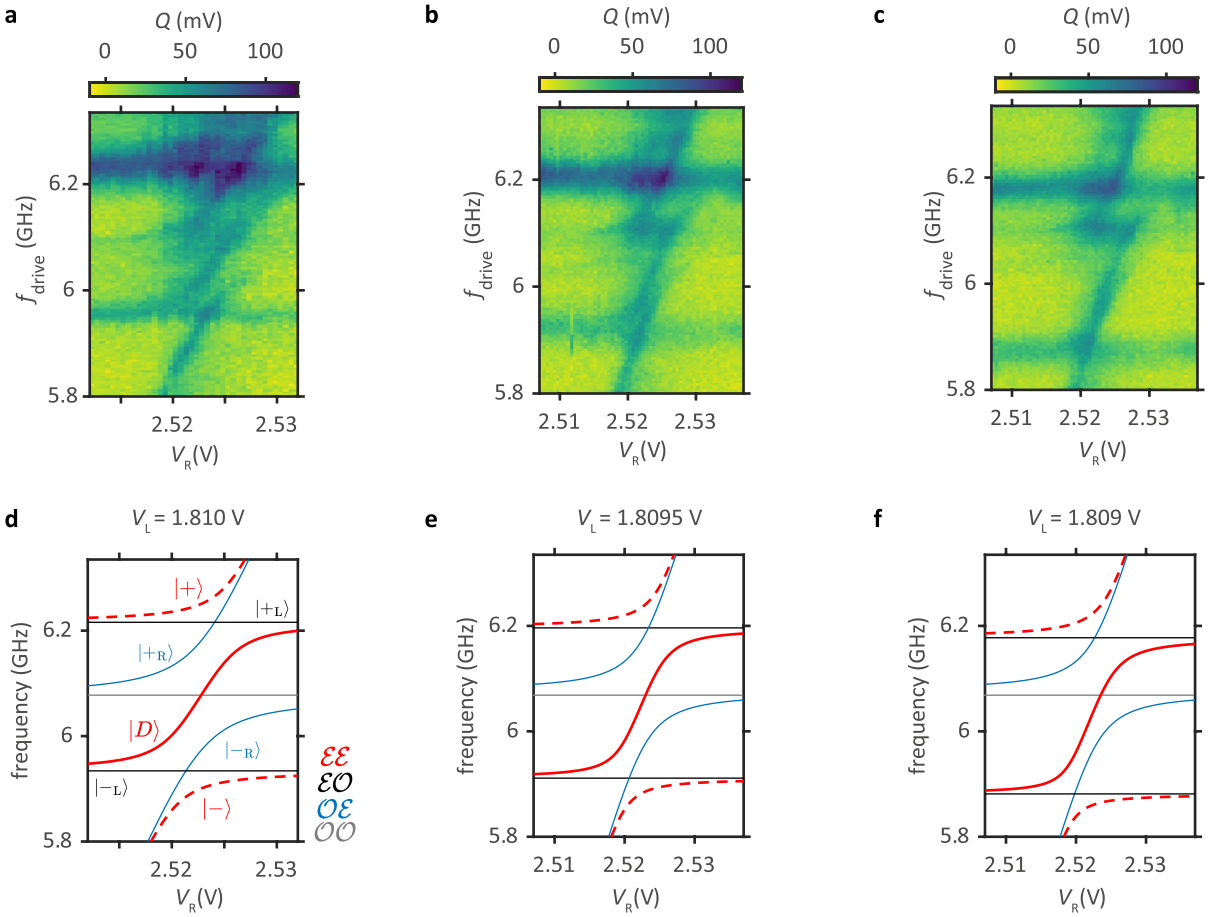

Extended Data Fig. 1 | Extended spectroscopy measurements of the full hybrid circuit at different V_L. a and **d** are also shown in the Fig. 3 in the main text. The spectra in **b** and **c** are measured by step-wise reducing V_L. **e** and **f** are calculated spectra using the Tavis-Cummings model with $f_{qb,L} = 0.993 f_a$ and $f_{qb,L} = 0.985 f_a$. Crucially, as the L-APQ is detuned from the anti-symmetric mode frequency f_a, the sigmoid-shaped two-qubit entangled state $|D\rangle$ (solid red) approaches the single APQ-coupler state $|-_R\rangle$ (blue) from the parity configuration $\mathcal{OE}$, in agreement to the measured spectra in **b** and **c**.

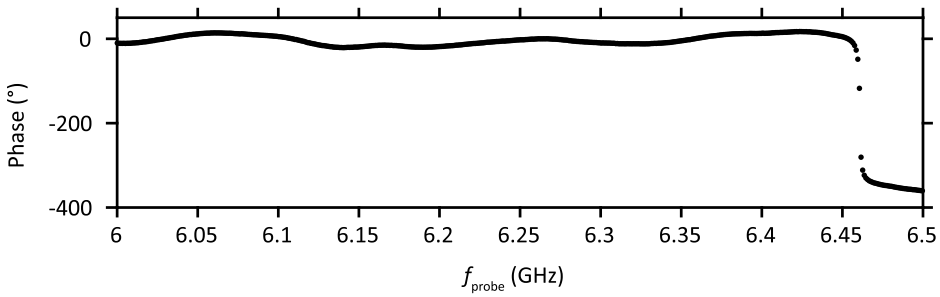

Extended Data Fig. 2 | Coupler spectrum. The phase of a weak microwave probe pulse as a function of the probe frequency f_{probe}. No phase shift is observed at 6.075 GHz, showing that the anti-symmetric coupler mode is weakly coupled to the readout port with considerably smaller κ_a. At 6.461 GHz, a phase shift of 360° is measured, which results from the reflection of the symmetric coupler mode.

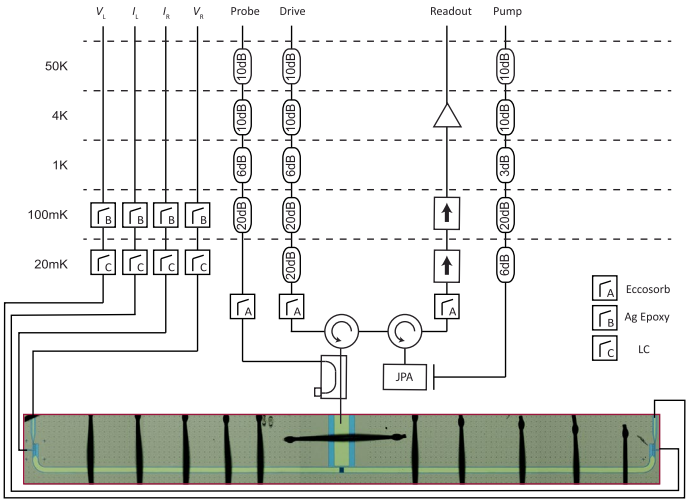

Extended Data Fig. 3 | Cryogenic wiring diagram. The qubit excitation and coupler probe pulses pass through the illustrated setup before being routed to the readout port on the chip. The probe pulse is reflected and then routed through the amplification chain containing a dimer Josephson-junction-array amplifier (JPA), a HEMT, and a room-temperature amplifier. An additional RF line is used to pump the JPA. The pump, drive and probe RF lines are filtered with eccosorb at the mixing chamber. The DC voltage and current lines are routed to the chip through Ag epoxy at the coldplate for thermal anchoring and three-stage LC filters with lowest cutoff frequencies at 80 MHz at the mixing chamber.